

Solution Processable Material Derived from Aromatic Triazole, Azomethine and Tris: Preparation and Hole-Buffering Application in Polymer Light-Emitting Diodes

Chih-Yang Lin, Yun Chen*

Department of Chemical Engineering, National Cheng Kung University, Taiwan

Email: *yunchen@mail.ncku.edu.tw

How to cite this paper: Lin, C.-Y. and Chen, Y. (2018) Solution Processable Material Derived from Aromatic Triazole, Azomethine and Tris: Preparation and Hole-Buffering Application in Polymer Light-Emitting Diodes. *Journal of Materials Science and Chemical Engineering*, 6, 6-28. <https://doi.org/10.4236/msce.2018.69002>

Received: August 31, 2018

Accepted: September 27, 2018

Published: September 30, 2018

Copyright © 2018 by authors and Scientific Research Publishing Inc.

This work is licensed under the Creative Commons Attribution International License (CC BY 4.0).

<http://creativecommons.org/licenses/by/4.0/>



Open Access

Abstract

This work presents the synthesis of a new hole-buffering material **TAZS** and its successful application in polymer light-emitting diodes to enhance device performance. The **TAZS** is composed of aromatic 1,2,4-triazolylcore linked with three trihydroxy *tert*-butyl terminals via azomethine linkages. The **TAZS** forms ashomogeneous film deposited by spin-coating process. The HOMO and LUMO levels of **TAZS** are -5.23 eV and -2.40 eV, respectively, as estimated from cyclic voltammogram. The current density results of hole-only and electron-only devices confirm strong hole-buffering capability of **TAZS** layer. Multilayer PLEDs with different thickness of **TAZS** (ITO/PEDOT: PSS/**TAZS** (x nm)/SY/ETL/LiF/Al) have been successfully fabricated, using spin-coating process to deposit hole-injecting PEDOT: PSS, **TAZS**, and emissive SY layers. The PLED with 16 nm **TAZS** reveals the optimal device performance, with maximum luminance and maximum current efficiency of $19,046$ cd/m² and 4.08 cd/A, respectively, surpassing those without **TAZS** as HBL (8484 cd/m², 2.13 cd/A). The hole-buffering characteristic of **TAZS** contributes greatly to improved charges' recombination ratio and enhanced emission efficiency.

Keywords

Hole-Buffering, Azomethine, Aromatic Triazole, Tris, Polymer Light-Emitting Diodes, Spin-Coating

1. Introduction

Polymer light-emitting diodes (PLEDs) [1] [2] [3] and organic light-emitting

diodes (OLEDs) [4] [5] [6] have drawn considerable attention due to numerous advantages such as self-luminous, wide view angle, and fast response time. Furthermore, PLEDs can be easily adapted for solution processes such as spin-coating and ink-jet printing which are appropriate processes for the fabrication of large-area and flexible displays [1] [2] [3]. Conversely, OLEDs was conventionally fabricated by thermal evaporation under vacuum, which is more costly and complicated. In general, balanced charge recombination in emission layer (EML) is essential for enhancement of device efficiency and stability. However, for most conjugated organic polymers and compounds applied in PLEDs holes transport more favorably than electrons [7] [8]. Therefore, efficient hole-buffering layer, which slows down hole-transport, is able to improve charge balance in EML. Some hole-buffering materials have been reported, such as copper(II) phthalocyanine (CuPC) and 4,4',4''-tris(N-carbazolyl)-triphenylamine (TATC) [9] [10]. They were inserted between hole injection layer and emission layer to reduce hole-transport effectively and improve the device performance [11]. We have prepared a hole-buffering polymer composed of alternating *p*-terphenyl and tetraethylene glycol ether, which effectively balance charges and device efficiency [12].

Formation of Schiff base is a nucleophilic addition of primary amine and aldehyde group, followed with dehydration to form as azomethine (-CH=N-). Schiff bases composed of azomethines have been reported during the past two decades as materials for organic optoelectronic application [12]-[19]. The azomethine bond possesses similar isoelectronic characteristics to vinyl bond, giving rise to similar optoelectronic and thermal properties [20] [21] [22]. However, most of the Schiff base derivatives prepared for OLED applications focused on phosphorescent luminescent materials [23] [24] [25] [26] [27]. To our knowledge, few studies focused on hole-buffering application for optoelectronic devices [15]. The fluorescence intensity of aromatic materials substituted with azomethine moieties is very weak due to quenching by photo-induced electron transfer (PET) [28] [29]. This characteristic is beneficiary for hole-buffering application in PLEDs, since its presence will not deteriorate color purity of the emission.

In this study, we synthesized a new azomethine-based molecule **TAZS** (aromatic 1,2,4-triazolyl as core) containing three peripheral trihydroxy *tert*-butyl groups. The bulky, polar trihydroxy *tert*-butyl groups not only increase solubility but also prevent aggregate formation during casting by wet processes. ¹H NMR, 2D COSY NMR, FT-IR, and mass spectrometry were used to characterize structure of **TAZS**. Multilayer PLEDs (ITO/PEDOT: PSS/**TAZS**/SY/ETL/LiF/Al) have been successfully fabricated by subsequent spin-coating of hole-injecting PEDOT: PSS layer, hole-buffer **TAZS** layer, and emissive SY layer. Insertion of **TAZS** as hole-buffer layer (HBL) effectively enhanced maximum luminance and maximum current efficiency to 19,046 cd/m² and 4.08 cd/A, respectively, from those without the HBL (8484 cd/m², 2.13 cd/A).

2. Experimental

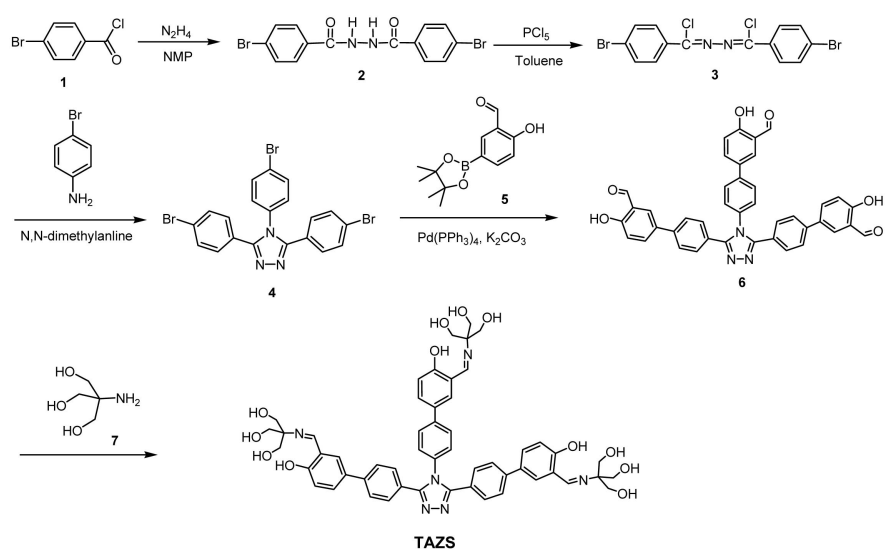
2.1. Synthesis of TAZS

All the reagents and materials were from commercial sources and used without further purification. Anhydrous tetrahydrofuran was obtained by refluxing with sodium under N₂ atmosphere overnight. **Scheme 1** depicts the detailed synthetic routes of **TAZS** from 4-bromobenzoyl chloride (**1**).

A mixture of 4-bromobenzoyl chloride (1:3.29 g, 15.0 mmol) in *n*-methylpyrrolidone (30 mL) was added hydrazine monohydrate (0.38 g, 7.5 mmol) under continuous stirring. The mixture was stirred at room temperature under N₂ atmosphere for 1 day. The mixture was poured into a large amount of water (200 mL), the appearing precipitate was collected by filtration, and then washed completely with ethyl acetate. The final product was dried under vacuum oven at 70 °C to obtain **2** (yield: 4.61 g, 77.2%). ¹H NMR (600 MHz, DMSO-d₆, ppm): δ 10.62 (s, 2H, -NH-), 7.85 - 7.84 (d, J = 8.6 Hz, 4H, Ar-H), 7.75 - 7.74 (d, J = 8.2 Hz, 4H, Ar-H).

A mixture of **2** (1.60 g, 4.0 mmol), phosphorus pentachloride (1.92 g, 9.3 mmol) and toluene (30 mL) was stirred at 120 °C for 3.5 hrs. After removal of toluene by a rotary evaporator, the crude product was washed with water, followed with drying in vacuum oven at 80 °C. The crude was recrystallized from ethanol and chloroform to obtain **3** (yield: 0.81 g, 46.3%). ¹H NMR (600 MHz, CDCl₃, ppm): δ 8.00 - 7.98 (d, J = 8.2 Hz, 4H, Ar-H), 7.62 - 7.60 (d, J = 8.2 Hz, 4H, Ar-H).

A mixture of **3** (0.86 g, 2.0 mmol), *p*-bromoaniline (0.34 g, 2.0 mmol) and *N,N*-dimethylaniline (15 mL) was stirred at 135 °C for 12 hrs. The reaction mixture was poured into 2N HCl_(aq) (30 mL) and the appearing solids were collected by filtration, washed with water and dried in vacuum oven at 80 °C. Then residues were recrystallized from H₂O and dimethyl sulfoxide (DMSO) to provide



Scheme 1. Synthetic routes of TAZS.

4 (yield: 0.77 g, 72.0%). ¹H NMR (600 MHz, DMSO-d₆, ppm): δ 7.69 - 7.67 (d, J = 8.1 Hz, 2H, Ar-H), 7.62 - 7.60 (d, J = 8.1 Hz, 4H, Ar-H), 7.40 - 7.38 (d, J = 8.0 Hz, 2H, Ar-H), 7.32 - 7.30 (d, J = 8.0 Hz, 4H, Ar-H).

To a two-necked flask were added with 5-bromo-2-hydroxybenzaldehyde (1.50 g, 7.5 mmol), potassium acetate (1.86 g, 18.9 mmol) and bis(pinacolato) diboron (2.31 g, 9.1 mmol). After adding [Pd(dppf)Cl₂] (0.36 g, 0.5 mmol) and THF (30 mL), the mixture was stirred at 70 °C for 18 hrs. After removing the solvent by a rotary evaporator, the residue was re-dissolved in dichloromethane, followed by extracting with water. The combined organic layer was concentrated by a rotary evaporator, then further purified by column chromatography using ethyl acetate and *n*-hexane (v/v = 1:12) as an eluent to obtain **5** (yield: 1.04 g, 56.1%). ¹H NMR (600 MHz, CDCl₃, ppm): δ 11.22 (s, 1H, -OH), 9.92 (s, 1H, -CH = O), 8.04 (d, 1H, Ar-H), 7.94 (dd, 1H, J = 8.2 Hz, Ar-H), 6.98 (d, 1H, J = 8.3 Hz, Ar-H), 1.35 (s, 12H, -CH₃).

To a two-necked flask were added with **4** (0.32 g, 0.6 mmol), **5** (0.60 g, 2.4 mmol) and [(*t*-Bu)₃PH]BF₄ (88.0 mg, 0.3 mmol). Then Pd (PPh₃)₄ (34.7 mg, 0.03 mmol), THF (20 mL) and K₂CO_{3(aq)} (2 M, 3 mL) were added under nitrogen atmosphere. The mixture was stirred at 70 °C for 24 hrs. It was poured into a large amount of water and then extracted with chloroform. The combined organic layer was collected and the solvent was removed using a rotary evaporator. The crude product was further purified by a column chromatograph using ethyl acetate and *n*-hexane (v/v = 2:1) as an eluent to obtain **6** (yield: 0.18 g, 46.4%). ¹H NMR (600 MHz, DMSO-d₆, ppm): δ 10.94 (s, 1H, -OH), 10.89 (s, 2H, -OH), 10.30 (s, 1H, -CH=O), 10.28 (s, 2H, -CH=O), 8.01 (s, 1H, Ar-H), 7.95 - 7.93 (m, 3H, Ar-H), 7.88 - 7.87 (d, J = 7.9 Hz, 2H, Ar-H), 7.82-7.81 (d, J = 8.5 Hz, 2H, Ar-H), 7.68 - 7.66 (d, J = 7.9 Hz, 4H, Ar-H), 7.58 - 7.56 (d, J = 8.5 Hz, 2H, Ar-H), 7.52 - 7.51 (d, J = 8.0 Hz, 4H, Ar-H), 7.11 - 7.09 (d, J = 8.5 Hz, 1H, Ar-H), 7.07 - 7.06 (d, J = 8.5 Hz, 2H, Ar-H).

A mixture of **6** (0.5 mmol, 0.33 g), 2-amino-2-(hydroxymethyl)-1,3-propanediol (tris, **7**: 2.05 mmol, 0.25 g) and methanol (50 mL) was stirred at 55 °C for 24 hrs. After removing methanol by a rotary evaporator, the resulted residue was washed successively with acetone and chloroform to obtain **TAZS** (yield: 0.44 g, 90.8%). ¹H NMR (600 MHz, DMSO-d₆, ppm): δ 14.73 (s, 1H), 14.69 (s, 2H), 8.62 (s, 1H, -NH-), 8.60 (s, 2H, -NH-), 7.87 (s, 1H, Ar-H), 7.82 - 7.80 (m, 4H, Ar-H), 7.72 - 7.71 (d, J = 8.4 Hz, 1H, Ar-H), 7.67 - 7.66 (m, 6H, Ar-H), 7.53 - 7.52 (d, J = 7.9 Hz, 2H, Ar-H), 7.49 - 7.48 (d, J = 7.9 Hz, 4H, Ar-H), 6.83 - 6.81 (d, J = 8.7 Hz, 1H, Ar-H), 6.79 - 6.78 (d, J = 8.8 Hz, 2H, Ar-H), 4.80 (m, 9H, -OH), 3.61 (m, 18H, -CH₂-).

2.2. General Procedures

The ¹H NMR and COSY NMR spectra were measured using a Bruker AV-600 MHz spectrometer, with the chemical shifts reported in ppm and using tetramethylsilane as the internal standard. The FT-IR spectra of compounds (in pellet form) were recorded with a Jasco FT-IR Spectrometer Volar III. Mass spectra

were measured with a mass spectrometer (Bruker Autoflex III TOF/TOF). Thermogravimetric analysis (TGA) of **TAZS** employed a PerkinElmer TGA-7 from 50 °C to 800 °C at a heating rate of 10 °C/min, under a nitrogen flow rate of 20 mL/min. The thermal decomposition temperature (T_d) is the temperature at 5% weight loss of the sample. Differential scanning calorimetric (DSC) measurements were conducted under nitrogen atmosphere, using a Mettler Toledo DSC 1 Star System, at heating rate of 10 °C/min. UV/Vis absorption spectra and photoluminescence (PL) spectra were recorded on a Jasco V-550 spectrophotometer and a Hitachi F-4500 fluorescence spectrophotometer, respectively. Cyclic voltammetry (CV) were carried out on a voltammetric apparatus (Model CV-50W) equipped with a three-electrode cell at a scan rate of 100 mV/s. The cell was composed of a carbon as the working electrode, Ag/AgNO₃ electrode as the reference electrode and a platinum wire as the auxiliary electrode. The electrodes were immersed in acetonitrile containing 0.1 M (*n*-Bu)₄NClO₄ as electrolyte. The energy levels were estimated using the ferrocene (FOC) value of -4.8 eV with respect to vacuum level, which is defined as zero. The onset potentials of oxidation and reduction were determined by the intersection of two tangent lines drawn at the background and rising current. Film thickness was measured with a surface profiler, alpha-step 500. Surface morphology of spin-coated films was measured with an atomic force microscope (AFM), equipped with a Veeco/Digital Instrument Scanning Probe Microscope (tapping mode) and a Nanoscope III controller.

2.3. Device Fabrication and Characterization

Indium tin oxide (ITO)-patterned glass substrate was consecutively cleaned using neutral detergent, deionized water, acetone and isopropyl alcohol, immersing in an ultrasonic bath at 50 °C, each for 20 min. In addition, the ITO substrate was rinsed with deionized water after each step. The cleaned ITO substrates were baked at 120 °C for 20 min to remove the deionized water. Finally, the cleaned ITOs were treated in an UV-ozone chamber for 20 min. A solution of PEDOT:PSS was spin-coated onto the ITO substrate at a spin rate of 3000 rpm and annealed at 150 °C for 20 min as a hole injection layer. A solution of **TAZS** in ethanol and DMF (*v/v* = 5/1) was spin-coated onto the PEDOT:PSS layer and annealed at 110 °C for 20 min to form as the hole-buffer layer (HBL). The concentration was 1.5 mg/mL, with the spin rate varying from 1000 rpm to 4000 rpm to obtain different film thickness. Then, the fluorescent poly (*para*-phenylene vinylene) derivative (Super Yellow PPV, SY, from Merck) was spin-coated at 4000 rpm on top of the **TAZS** layer and annealed at 70 °C for 20 min to construct the emission layer (EML). Finally, LiF (1 nm) and Al (90 nm) was subsequently vacuum deposited on top of the EML as the cathode. The luminance-voltage, current density-voltage relationships and electroluminescence spectra (EL) of the multilayer PLEDs were recorded using a combination of the Keithley source-meter (model 2400) and an Ocean Optics usb2000 fluorescence spectrophotometer. The thickness of deposited films was measured using a sur-

face profiler, alpha-step 500.

3. Results and Discussion

3.1. Synthesis and Characterization

Scheme 1 depicts the detailed synthetic procedures of **TAZS** from 4-bromobenzoyl chloride (**1**) within five steps. The ^1H NMR spectra of intermediates (**2**, **3**, **4**, **5**) are attached as **Figures S1-S4** in Supplementary Information. Chemical structures of **2** - **5** were satisfactorily confirmed by the ^1H NMR in which the protons were easily assigned. Compound **6** with three benzaldehyde peripherals was synthesized from 3,4,5-tri(4-bromophenyl)-4H-1,2,4-triazole (**4**) and 2-hydroxy-5-(4,4,5,5-tetramethyl-1,3,2-dioxaborolan-2-yl) benzaldehyde (**5**) by the Suzuki coupling reaction. The ^1H NMR and 2D COSY spectra of **6** are also provided as **Figure S5** and **Figure S6**. All protons were successfully assigned using the 2D COSY spectra (**Figure S6**) and its structure was satisfactorily confirmed based on the integral areas of the protons (**Figure S5**). Finally, the target **TAZS** with three azomethine linkages was synthesized by the Schiff base-forming condensation of **6** and 2-amino-2-(hydroxymethyl)-1,3-propanediol(**7**: tris). The purpose of attaching high polar trihydroxy *tert*-butyl groups is to improve the solubility of **TAZS** in protic solvents such as alcohol. **Figure 1** shows the ^1H NMR spectrum of **TAZS**, with all the proton peaks assigned by the 2D COSY NMR spectrum (**Figure S7**). The FTIR spectrum confirmed successful formation of azomethine linkages by the presence of C=N vibrational absorption peak at 1633 cm^{-1} and a broad band of hydroxyl groups at 3310 cm^{-1} (**Figure S8**). The MALDI/TOF-MS spectra of **6** and **TAZS** are demonstrated in **Figure S9** and **Figure S10** and **Figure S11** and **Figure S12**, respectively. The largest molecular masses (m/z) of **6** and **TAZS** were 658.02 (**Figure S9**) and 967.23 (**Figure S11**), respectively, which are very close to true molecular weights (657.67, 967.03).

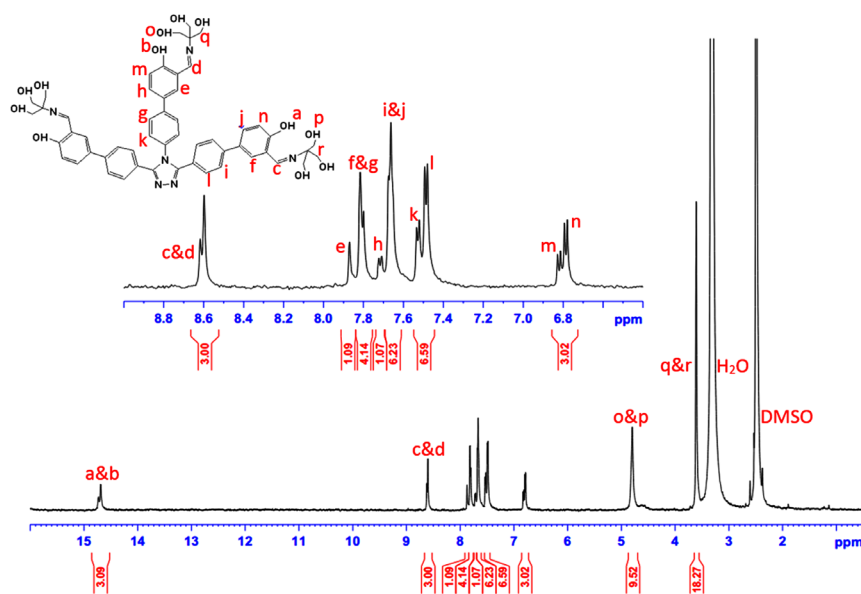


Figure 1. ^1H NMR spectrum of **TAZS** in DMSO-d_6 .

3.2. Thermal and Optical Properties of TAZS

Thermal decomposition and transition properties of **TAZS** were investigated using a thermogravimetric analytical apparatus (TGA) and a differential scanning calorimeter (DSC), respectively, at a scanning rate of 10 °C/min and under a nitrogen atmosphere. **TAZS** reveals a two-step thermal decomposition (**Figure S13(a)**) and the thermal decomposition temperature (T_d) is 264 °C (at 5% weight loss). The first-step decomposition of **TAZS** is attributable to the thermal degradation of peripheral trihydroxy *tert*-butyl groups. The second stage would be the decomposition of aromatic chromophores. Furthermore, the residue at 800 °C was still high at *ca.* 43%, which is probably owing to thermal carbonization of rigid aromatic core including triazolyl group. However, **TAZS** does not exhibit any thermal transitions up to 200 °C, as shown in **Figure S13(b)**, suggesting that it is amorphous material in film state. The bulky trihydroxy *tert*-butyl terminals and high twist angle between triazolyl core and phenyl groups prevent the crystallization process during film casting. Amorphous material is highly required for PLEDs because it effectively reduces performance degradation caused by crystallization during device operation.

Figure 2 shows the normalized UV/Visible absorption and photoluminescence (PL) spectra of **TAZS** in ethanol solution and in film state, with the characteristic data summarized in **Table 1**. In ethanol, the main absorption maximum of **TAZS** is peaked at 315 nm, with a smaller peak located at 421 nm. The

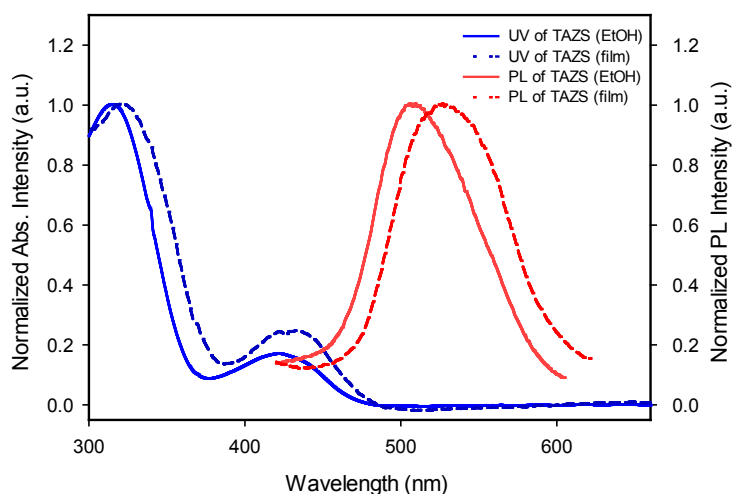


Figure 2. Normalized absorption spectra and photoluminescence spectra of **TAZS** in ethanol solution (–) and in the film state (---).

Table 1. Optical properties of **TAZS**.

	UV/Vis λ_{\max} (nm)		PL λ_{\max} (nm)		E_g^{opt} (eV) ^c
	Solution ^a	Film ^b	Solution ^a	Film ^b	
TAZS	315, 421	321, 433	509	527	3.24

^aIn 10⁻⁵ Methanol solution. ^bThe films were obtained by spin-coating (1000 rpm) their solutions (5 mg/mL in DMF). ^cThe value was estimated by the λ_{onset} of the UV/Vis spectra.

main absorption of **TAZS** is attributed to the π - π^* transitions of conjugated moieties, whereas the absorption band at 421 nm is attributable to the n - π^* transitions of conjugated region including terminal azomethines. The PL intensity of **TAZS** is extremely low in both solution and film state (the PL spectra in **Figure 2** is after normalization). This is because of significant fluorescence quenching due to the photo-induced electron transfer (PET) from azomethine groups [28] [29]. Non-emissive HBL is beneficial to high color purity, because even slight emission from HBL may deteriorate emission color. The PL spectra of **TAZS** in the ethanol and solid state are located at 509 nm and 527 nm, respectively. The absorption and PL maxima of **TAZS** in solid state are red-shifted slightly relative to those in ethanol solution. The redshift is probably owing to molecular aggregation caused by stronger intermolecular interactions.

3.3. Electrochemical Properties

Cyclic voltammetric apparatus has been constantly employed to measure the electrochemical properties, especially onset oxidation and reduction potentials, of organic and polymeric materials. The highest occupied molecular orbital (HOMO) and lowest unoccupied molecular orbital (LUMO) energy levels are readily estimated from the onset oxidation and reduction potentials, respectively. **Figure 3** demonstrates the cyclic voltammogram (CV) of **TAZS** and **Table 2** summaries corresponding electrochemical data. The CV curve was not a closed loop, probably attributed to the equilibrium between **TAZS** and electrolyte ion

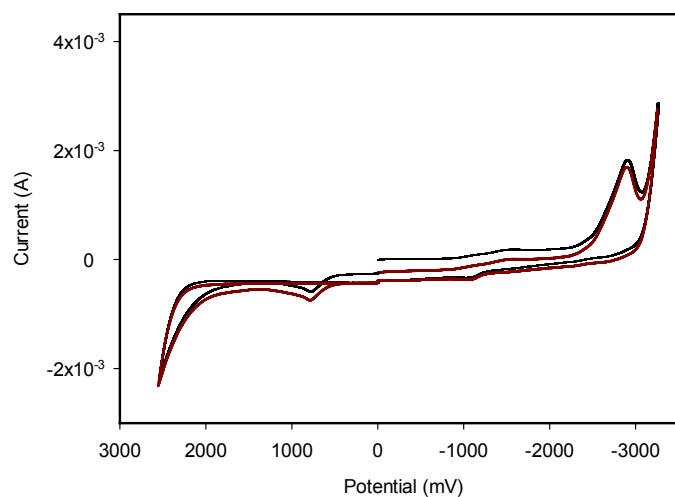


Figure 3. Cyclic voltammogram of TAZS in 0.1 M $(n\text{-Bu})_4\text{NClO}_4$; scan rate: 100 mV/s.

Table 2. Electrochemical properties of **TAZS**.

	$E_{\text{onset(ox) vs. FOC}}$ (V) ^a	$E_{\text{onset(red) vs. FOC}}$ (V) ^a	E_{HOMO} (eV) ^b	E_{LUMO} (eV) ^c	E_{g}^{el} (eV) ^d	$E_{\text{g}}^{\text{opt}}$ (eV) ^e
TAZS	0.43	-2.40	-5.23	-2.40	2.83	3.24

^a $E_{\text{polymer}} = 0.07$ V vs. Ag/AgNO₃. ^b $E_{\text{HOMO}} = -(E_{\text{onset(ox), FOC}} + 4.8)$ eV. ^c $E_{\text{LUMO}} = -(E_{\text{onset(red), FOC}} + 4.8)$ eV. ^d $E_{\text{g}} = [\text{LUMO} - \text{HOMO}]$. ^e $E_{\text{g}} = 1240/\lambda_{\text{onset abs}}$ (nm).

was still not established. The estimated HOMO and LUMO levels of **TAZS** are -5.23 eV and -2.40 eV, respectively, leading to a bandgap of 2.83 eV. This bandgap is much lower than the optically estimated one ($E_g^{\text{opt}} = 3.24$ eV), due probably to the bipolar characteristic of **TAZS**. The oxidation starts from electron-rich azomethine moiety, while the reduction begins from electron-withdrawing triazolyl core. Accordingly, the electrochemically estimated bandgap (E_g^{el}) is much lower than that calculated from onset absorption (E_g^{opt}). **Figure 4** demonstrates the energy band diagrams of composition layers in multilayer PLEDs (ITO/PEDOT: PSS/**TAZS**/SY/LiF/Al). The HOMO level of **TAZS** (-5.23 eV) is deeper than -5.0 eV of PEDOT: PSS; thus there is a barrier height ($\Delta E_h = 0.23$ eV) at the interface of **TAZS** and hole-injecting PEDOT: PSS layers. Accordingly, the presence of **TAZS** layer will reduce injection/transport rate of holes. In addition, the LUMO level (-2.40 eV) of **TAZS** is higher than -2.8 eV of SY emissive layer to result in a barrier height in the interface. Moreover, electron-withdrawing triazolyl core tends to obstruct holes' transport. Therefore, **TAZS** is expected to be an effective hole-buffer layer in PLEDs to raise charges' recombination ratio that results in enhanced emission efficiency.

3.4. Morphological Properties

Film homogeneity of compositional layers, whether in OLEDs or PLEDs, is an essential prerequisite to obtain efficient and reproducible devices. When use wet processes such as spin coating or inkjet printing to deposit film, polymers usually give rise to more homogeneous film than low molecular weight compounds. This is because of intrinsic film-forming property of polymers attributable to high molecular weight. On the contrary, the film-forming property of low molecular compounds is usually poor by solution processes. However, as illustrated in **Figure 5**, the surface morphologies of **TAZS** obtained from atomic force microscopy (AFM) were quite smooth. The root-mean-square (rms) surface roughness were between 1.90 to 3.33 nm (**Table 3**), compared with 1.20 nm of

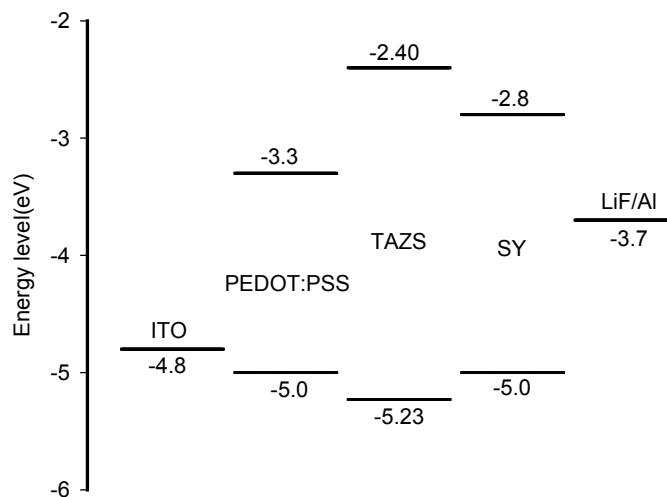


Figure 4. Energy band diagrams of PLEDs (ITO/PEDOT: PSS/**TAZS**/SY/LiF/Al).

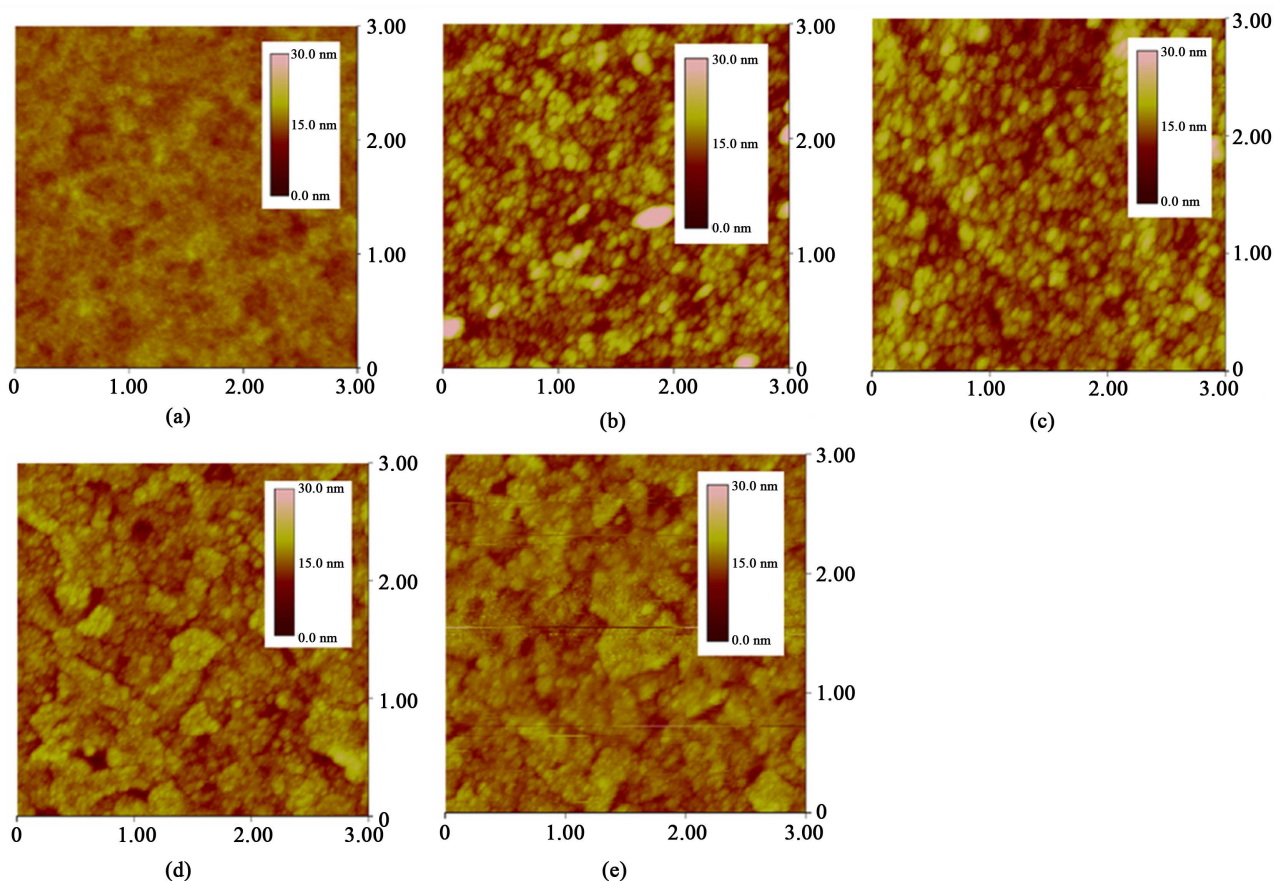


Figure 5. AFM images of (a) PEDOT: PSS and (b)-(e) TAZS on the top of PEDOT: PSS film deposited at different spin rate. Spin rate: (b) 1000; (c) 2000; (d) 3000; (e) 4000 rpm.

Table 3. Thickness and roughness of films deposited at different spin rates^a.

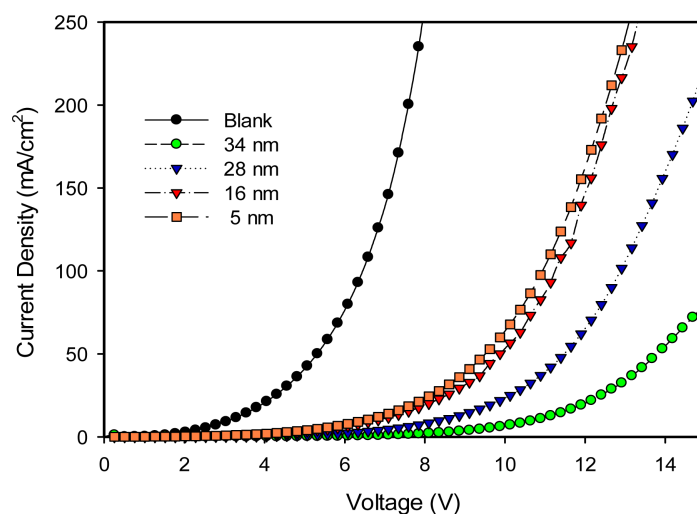
Deposited films	Spin rate (rpm)	Thickness (nm)	Roughness (nm) ^b
PEDOT: PSS	3000	40	1.20
	1000	34	3.33
TAZS ^a	2000	28	2.75
	3000	16	2.00
	4000	5	1.90

^aFilms were obtained by spin-coating of **TAZS** solution in EtOH and DMF (v/v = 5/1); the concentration was 1.5 mg/mL. ^bRoot-mean-square (rms) surface roughness.

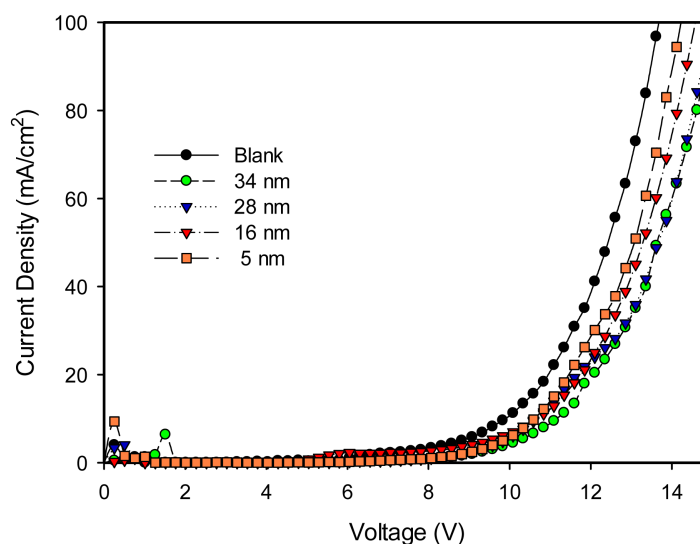
the underlying PEDDOT: PSS layer. Moreover, the roughness decreased from 3.33 nm to 1.90 nm with spin rate increasing from 1000 rpm to 4000 rpm. The bulky trihydroxy *tert*-butyl groups on the periphery of **TAZS** are effective to prevent extreme aggregation in film state. This is coincident with previous result obtained in DSC investigation, which confirmed the amorphous phase of **TAZS** in solid state. Amorphous materials usually lead to better homogeneous morphology when deposited by solution processes.

3.5. Single-Carrier Transporting Property

In order to evaluate charge-transporting properties of multilayer PLEDs in the presence of TAZS layer, we fabricated single-carrier (hole-only and electron-only) devices by appropriate selection of cathode and anode metals, respectively. The hole-only device (HOD), ITO/PEDOT: PSS/TAZS/SY/LiF/Au, used high work function Au (-5.1 eV) as the cathode instead of aluminum (Al). High work-function Au cathode restricts electron injection; therefore, holes contribute exclusively to current density. The electron-only device (EOD), Glass/PEDOT: PSS/Ag/TAZS/SY/LiF/Al, employed silver (Ag) as the anode to prevent hole injection into EML [30] [31]. The function of PEDOT: PSS layer was to smooth the surface of ITO glass. **Figure 6** depicts current density versus



(a)



(b)

Figure 6. (a) Current density versus voltage characteristics for HOD with and without TAZS layer; (b) Current density versus voltage characteristics for EOD with and without TAZS layer.

voltage of the single carrier devices. For blank devices without **TAZS** layer, the current density of HOD is much higher than that of EOD under the same operating voltage. For instance, at 6.0 V the current density was *ca.* 75 mA/cm² for HOD; however, it was almost non-detectable for EOD. Apparently, holes transport much faster than electrons in these PLEDs, leading to low charge recombination ratio and degraded emission efficiency. Therefore, reduction of holes' transport is necessary to raise charge recombination ratio and emission efficiency.

For hole-only devices, current density decreases dramatically after the insertion of **TAZS** layer (**Figure 6(a)**), confirming its hole-buffering capability. Moreover, the reduction in current density increases greatly with thickness from 5 nm to 34 nm. On the other hand, for electron-only devices the current density decreases only slightly in the presence of **TAZS** layer (**Figure 6(b)**). From the results of single-carrier devices, it is clear that the **TAZS** layer reveals mainly hole-buffering capability to raise charges' recombination ratio and emission efficiency.

3.6. Electroluminescent Properties

To determine the applicability of **TAZS** as hole-buffer layer (HBL), multilayer PLEDs were fabricated with a device structure of ITO/PEDOT: PSS/**TAZS**/SY/LiF/Al. The PEDOT: PSS is conventional hole-injection layer, while the Super Yellow (SY) was employed as the fluorescent emitter. The hole-buffering **TAZS** layer was deposited between hole-injection PEDOT: PSS and emissive SY layers. All of the organic layers, including PEDOT: PSS, **TAZS** and SY, were deposited by spin-coating process. The thickness of **TAZS** layer varied from 5 nm to 34 nm, depending on the spin rates (**Table 3**). **Figure 4** demonstrates the energy level diagram of composition layers in the PLEDs. The **TAZS** (−5.23 eV) has a HOMO level deeper than SY (−5.0 eV), with a barrier height of 0.23 eV for holes. In addition, as mentioned above, the electron-withdrawing aromatic 1,2,4-triazolyl moieties reduce transport of holes. This indicates that **TAZS** acts mainly as hole-buffering layer.

Figure 7 presents the luminance-voltage, current density-voltage characteristics, and current efficiency versus current density of the multilayer PLEDs, with the corresponding data summarized in Table. Insertion of **TAZS** layer leads to obvious reduction in current density and increase in turn-on voltage (**Figure 7(b)**, **Table 4**). This is attributable to the hole-buffering effect of the **TAZS** layer. However, the maximum luminance, maximum current efficiency, and maximum luminous power efficiency reveal significant enhancement except for the device with 34 nm of **TAZS** layer. For instance, at 16 nm **TAZS** layer the luminance and current efficiency are optimal at 19,046 cd/m² and 4.08 cd/A, respectively. The device performance is superior to that of the blank without the **TAZS** layer (8,484 cd/m², 2.13 cd/A). Dramatic performance degradation at thicker **TAZS** (34 nm) is probably ascribed to imbalanced charges' recombination caused by over-reduction in holes' transport. However, regardless of the

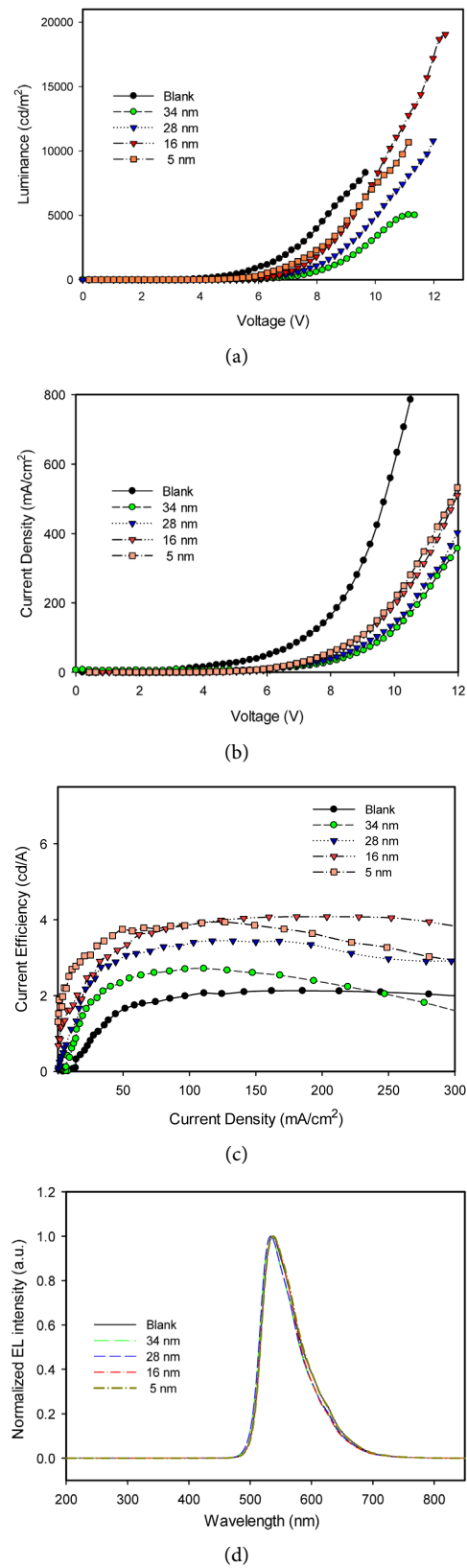


Figure 7. (a) Luminance versus voltage; (b) Current density versus voltage; (c) Current efficiency versus current density, and EL spectra of PLEDs. Device structure: ITO/PEDO: PSS (40 nm)/TAZS (x nm)/SY (70 nm)/LiF (1 nm)/Al (90 nm).

Table 4. Optoelectronic properties of PLEDs with hole-buffering **TAZS** layer^a.

Thickness of TAZS	V _{on} (V) ^b	L _{max} (cd/m ²) ^c	CE _{max} (cd/A) ^d	LPE _{max} (lm/W) ^e	CIE (x, y) ^f
None	3.4	8484	2.13	0.88	(0.41, 0.57)
5 nm ^g	4.1	10,664	3.93	1.51	(0.41, 0.57)
16 nm ^g	4.5	19,046	4.08	1.38	(0.40, 0.58)
28 nm ^g	5.3	10,770	3.44	1.14	(0.39, 0.58)
34 nm ^g	5.7	6574	2.71	0.88	(0.42, 0.56)

^aDevice structure: ITO/PEDOT: PSS (40 nm)/**TAZS** (x nm)/SY (70 nm)/LiF (1 nm)/Al (90 nm). ^bTurn-on voltage at 10 cd/m². ^cMaximum luminance. ^dMaximum current efficiency. ^eMaximum luminous power efficiency. ^fThe 1931 CIE coordinate at maximum luminance. ^gThickness was measured by alpha-step.

TAZS thickness, the emission spectra remains almost unchanged as shown in **Figure 7(d)** and in CIE coordinates in **Table 4**. This indicates that the recombination region of holes and electrons is mainly in the emissive SY layer. Accident exciton formation in **TAZS** layer near interface will not degrade color purity, because the emission of **TAZS** is negligible due to fluorescent quenching by induced electron transfer from azomethine groups [28] [29]. To conclude, hole-buffering capability of **TAZS** layer effectively raise the recombination ratio of carriers in PLEDs to improve carriers' recombination ratio, leading to enhanced device performance.

4. Conclusion

We have successfully synthesized a new aromatic 1,2,4-triazolylderivative (**TAZS**) linked with three peripheral trihydroxy *tert*-butyl groups via azomethine bond. The **TAZS** is an amorphous material with thermal decomposition temperature of 264°C. Moreover, **TAZS** reveals as homogeneous film by spin-coating process. Insertion of **TAZS** layer between hole-injecting PEDOT: PSS and emission SY layers dramatically reduces current density of hole-only devices, but only slightly for electron-only devices. Multilayer PLEDs have been successfully fabricated using 5 - 34 nm spin-coated **TAZS** as hole-buffer layer (HBL). The PLED with 16 nm **TAZS** demonstrates the optimal performance, with maximum luminance and maximum current efficiency of 19,046 cd/m² and 4.08 cd/A, respectively. Both luminance and efficiency are significantly enhanced when compared to the device without HBL (8484 cd/m², 2.13 cd/A).

Acknowledgements

The authors gratefully acknowledge financial support from the Ministry of Science and Technology of Taiwan (MOST106-2221-E-006-209).

Conflicts of Interest

The authors declare no conflicts of interest regarding the publication of this paper.

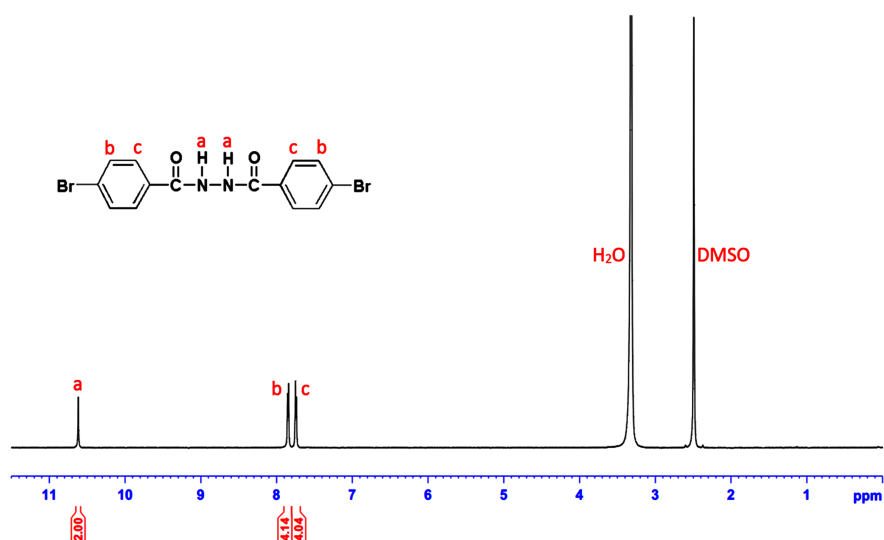
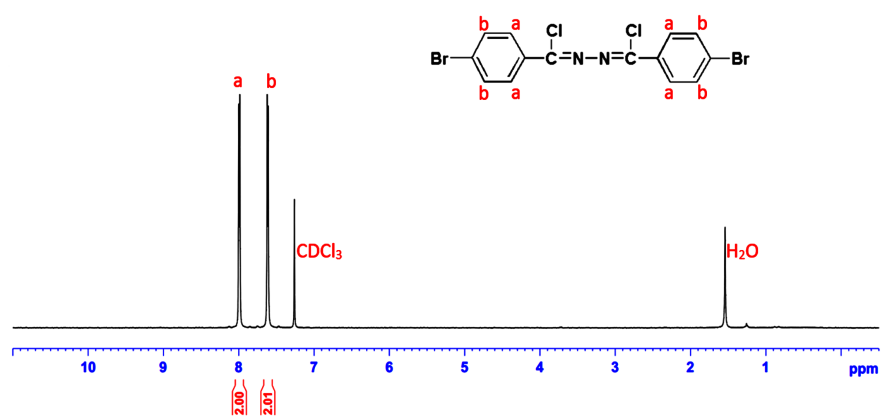
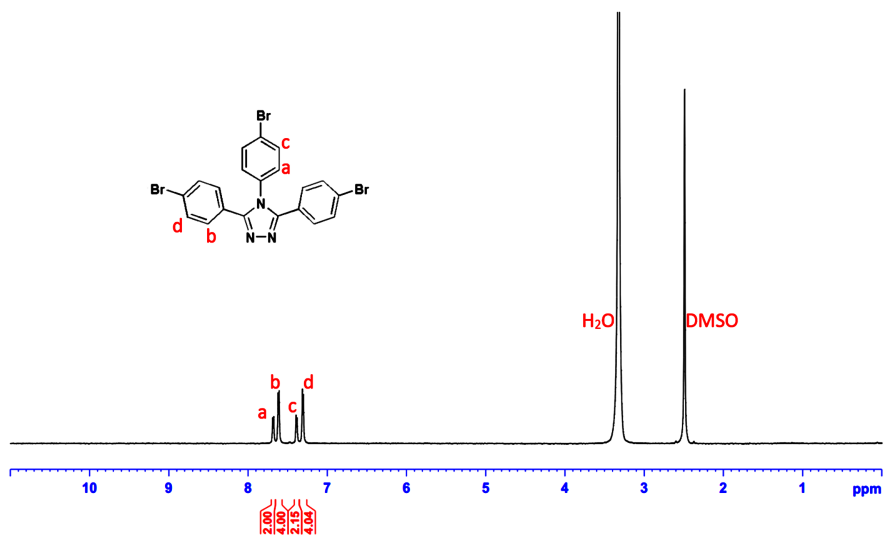
References

- [1] Friend, R.H., Gymer, R.W., Holmes, A.B., Burroughes, J.H., Marks, R.N., Taliani, C., Bradley, D.D.C., Dos Santos, D.A., Bredas, J.L., Logdlund, M. and Salaneck, W.R. (1999) Electroluminescence in Conjugated Polymers. *Nature*, **397**, 121-128. <https://doi.org/10.1038/16393>
- [2] Gustafsson, G., Cao, Y., Treacy, G.M., Klavetter, F., Colaneri, N. and Heeger, A.J. (1992) Flexible Light-Emitting-Diodes Made from Soluble Conducting Polymers. *Nature*, **357**, 477-479. <https://doi.org/10.1038/357477a0>
- [3] Burroughes, J.H., Bradley, D.D.C., Brown, A.R., Marks, R.N., Mackay, K., Friend, R.H., Burn, P.L. and Holmes, A.B. (1990) Light-Emitting-Diodes Based on Conjugated Polymers. *Nature*, **347**, 539-541. <https://doi.org/10.1038/347539a0>
- [4] Tsujimura, T. (2017) OLED Display Fundamentals and Applications. Wiley-SID Series in Display Technology, New York. <https://doi.org/10.1002/9781119187493>
- [5] Kamtekar, K.T., Monkman, A.P. and Bryce, M.R. (2010) Recent Advances in White Organic Light-Emitting Materials and Devices (WOLEDs). *Advanced Materials*, **22**, 572-582. <https://doi.org/10.1002/adma.200902148>
- [6] Shinar, J. (2004) Organic Light-Emitting Devices: A Survey. Springer-Verlag, New York. <https://doi.org/10.1007/978-0-387-21720-8>
- [7] Malliaras, G.G. and Scott, J.C. (1998) The Roles of Injection and Mobility in Organic Light Emitting Diodes. *Journal of Applied Physics*, **83**, 5399-5403. <https://doi.org/10.1063/1.367369>
- [8] Meng, H.-F. and Chen, Y.-S. (2004) Theory of Imbalanced Electron-Hole Transport in Conjugated Polymers. *Physical Review B*, **70**, Article ID: 115208. <https://doi.org/10.1103/PhysRevB.70.115208>
- [9] Xia, Y.-J., Lin, J., Tang, C., Yin, K., Zhong, G.-Y., Ni, G., Peng, B., Gan, F.-X. and Huang, W. (2006) High-Efficiency Blue-Emitting Organic Light-Emitting Devices with 4,4',4''-Tris(N-Carbazolyl)-Triphenylamine as the Hole/Exciton-Blocking Layer. *Journal of Physics D: Applied Physics*, **39**, 4987. <https://doi.org/10.1088/0022-3727/39/23/013>
- [10] Tadayyon, S.M., Grandin, H.M., Griffiths, K., Norton, P.R., Aziz, H. and Popovic, Z.D. (2004) CuPc Buffer Layer Role in OLED Performance: A Study of the Interfacial Band Energies. *Organic Electronics*, **5**, 157-166. <https://doi.org/10.1016/j.orgel.2003.10.001>
- [11] Lee, S.J., Lee, S.E., Lee, D.H., Koo, J.R., Lee, H.W., Yoon, S.S., Park, J. and Kim, Y.K. (2014) Effect of Broad Recombination Zone in Multiple Quantum Well Structures on Lifetime and Efficiency of Blue Organic Light-Emitting Diodes. *Japanese Journal Applied Physics*, **53**, Article ID:101601. <https://doi.org/10.7567/JJAP.53.101601>
- [12] Sek, D., Siwy, M., Grucela, M., Malecki, G., Nowak, E.M., Lewinska, G., Santera, J., Laba, K., Lapkowski, M., Kotowicz, S. and Schab-Balcerzak, E. (2017) New Anthracene-Based Schiff Bases: Theoretical and Experimental Investigations of Photo-physical and Electrochemical Properties. *Spectrochimica Acta Part A: Molecular and Biomolecular Spectroscopy*, **175**, 24-35. <https://doi.org/10.1016/j.saa.2016.12.013>
- [13] Sek, D., Grucela-Zajac, M., Krompiec, M., Janeczek, H. and Schab-Balcerzak, E. (2012) New Glass Forming Triarylamine Based Azomethines as a Hole Transport materials: Thermal, Optical and Electrochemical Properties. *Optical Materials*, **34**, 1333-1346. <https://doi.org/10.1016/j.optmat.2012.02.014>
- [14] Sęk, D., Lapkowski, M., Dudek, H., Karoń, K., Janeczek, H. and Jarzabek, B. (2012) Optical and Electrochemical Properties of Three-Dimensional Conjugated Triphe-

- nylamine-Azomethine Molecules. *Synthetic Metals*, **162**, 1046-1051.
<https://doi.org/10.1016/j.synthmet.2012.04.024>
- [15] Wesley Jeevadason, A., KalidasaMurugavel, K. and Neelakantan, M.A. (2014) Review on Schiff Bases and Their Metal Complexes as Organic Photovoltaic Materials. *Renewable & Sustainable Energy Reviews*, **36**, 220-227.
<https://doi.org/10.1016/j.rser.2014.04.060>
- [16] Abu-Dief, A.M. and Mohamed, I.M.A. (2015) A Review on Versatile Applications of Transition Metal Complexes Incorporating Schiff Bases. *Beni-Suef University Journal of Basic and Applied Sciences*, **4**, 119-133.
<https://doi.org/10.1016/j.bjbas.2015.05.004>
- [17] Sánchez, C.O., Bèrnede, J.C., Cattin, L., Makha, M. and Gatica, N. (2014) Schiff Base Polymer Based on Triphenylamine Moieties in the Main Chain. Characterization and Studies in Solar Cells. *Thin Solid Films*, **562**, 495-500.
<https://doi.org/10.1016/j.tsf.2014.04.071>
- [18] Petrus, M.L., Bouwer, R.K.M., Lafont, U., Athanasopoulos, S., Greenham, N.C. and Dingemans, T.J. (2014) Small-Molecule Azomethines: Organic Photovoltaics via Schiff Base Condensation Chemistry. *Journal of Materials Chemistry A*, **2**, 9474-9477.
<https://doi.org/10.1039/C4TA01629G>
- [19] Iwan, A., Schab-Balcerzak, E., Grucela-Zajac, M. and Skorka, L. (2014) Structural Characterization, Absorption and Photoluminescence Study of Symmetrical Azomethines with Long Aliphatic Chains. *Journal of Molecular Structure*, **1058**, 130-135. <https://doi.org/10.1016/j.molstruc.2013.10.067>
- [20] Morgan, P.W., Kwolek, S.L. and Pletcher, T.C. (1987) Aromatic Azomethine Polymers and Fibers. *Macromolecules*, **20**, 729-739.
<https://doi.org/10.1021/ma00170a006>
- [21] Kuder, J.E., Gibson, H.W. and Wychick, D. (1975) Linear Free Energy Relations. III. Electrochemical Characterization of Salicylaldehyde Anils. *Journal of Organic Chemistry*, **40**, 875-879. <https://doi.org/10.1021/jo00895a013>
- [22] Guarin, S.A.P., Bourgeaux, M., Dufresne, S. and Skene, W.G. (2007) Photophysical, Crystallographic, and Electrochemical Characterization of Symmetric and Unsymmetric Self-Assembled Conjugated Thiopheno Azomethines. *Journal of Organic Chemistry*, **72**, 2631-2643. <https://doi.org/10.1021/jo070100o>
- [23] Zhou, L., Kwong, C.L., Kwok, C.C., Cheng, G., Zhang, H. and Che, C.M. (2014) Efficient Red Electroluminescent Devices with Sterically Hindered Phosphorescent Platinum (II) Schiff Base Complexes and Iridium Complex Codopant. *Chemistry*, **9**, 2984-2994. <https://doi.org/10.1002/asia.201402618>
- [24] Nishal, V., Singh, D., Kumar, A., Tanwar, V., Singh, I., Srivastava, R. and Kadyan, P.S. (2014) A New Zinc-Schiff Base Complex as an Electroluminescent Material. *Journal of Organic Semiconductors*, **2**, 15-20.
<https://doi.org/10.1080/21606099.2014.942767>
- [25] Kathirgamanathan, P., Surendrakumar, Antipan-Lara, J., Ravichandran, R., Chan, Y.F., Arkley, V., Ganeshamurugan, S., Kumaravel, M., Paramswara, G., Partheepan, A., Reddy, V.R., Bailey, D. and Blake, A.J. (2012) Novel Lithium Schiff-Base Cluster Complexes as Electron Injectors: Synthesis, Crystal Structure, Thin Film Characterisation and Their Performance in OLEDs. *Journal of Materials Chemistry*, **22**, 6104-6116. <https://doi.org/10.1039/c2jm15114f>
- [26] Che, C.M., Kwok, C.C., Lai, S.W., Rausch, A.F., Finkenzeller, W.J., Zhu, N. and Yersin, H. (2010) Photophysical Properties and OLED Applications of Phosphorescent Platinum (II) Schiff Base Complexes. *Chemistry*, **16**, 233-247.

- <https://doi.org/10.1002/chem.200902183>
- [27] Wang, L., Jiao, S., Zhang, W., Liu, Y. and Yu, G. (2013) Synthesis, Structure, Optoelectronic Properties of Novel Zinc Schiff-Base Complexes. *Chinese Science Bulletin*, **58**, 2733-2740. <https://doi.org/10.1007/s11434-013-5786-2>
- [28] Sariciftci, N.S., Smilowitz, L., Heeger, A.J. and Wudl, F. (1992) Photoinduced Electron-Transfer from a Conducting Polymer to Buckminsterfullerene. *Science*, **258**, 1474-1476. <https://doi.org/10.1126/science.258.5087.1474>
- [29] Gupta A. and Kumar, N. (2016) A Review of Mechanisms for Fluorescent “Turn-On” Probes to Detect Al³⁺ Ions. *RSC Advances*, **6**, 106413-106434. <https://doi.org/10.1039/C6RA23682K>
- [30] Manabe, K., Hu, W., Matsumura, M. and Naito, H. (2003) Transport of Carriers in Organic Light-Emitting Devices Fabricated with a p-Phenylenevinylene-Derivative Copolymer. *Journal of Applied Physics*, **94**, 2024-2027. <https://doi.org/10.1063/1.1586964>
- [31] Steyrlleuthner, A., Bange, S. and Neher, D. (2009) Reliable Electron-Only Devices and Electron Transport in *n*-Type Polymers. *Journal of Applied Physics*, **105**, Article ID: 064509. <https://doi.org/10.1063/1.3086307>

Supplementary Information

Figure S1. ¹H NMR spectrum of compound 2.Figure S2. ¹H NMR spectrum of compound 3.Figure S3. ¹H NMR spectrum of compound 4.

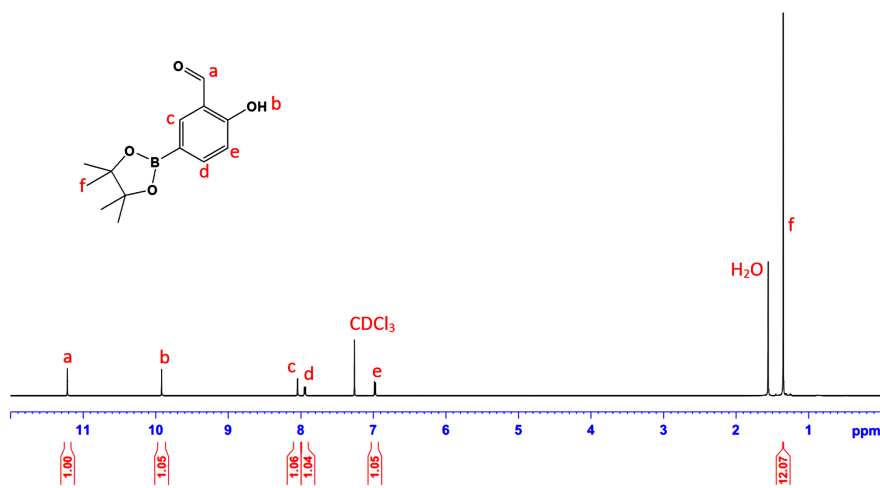


Figure S4. ¹H NMR spectrum of compound 5.

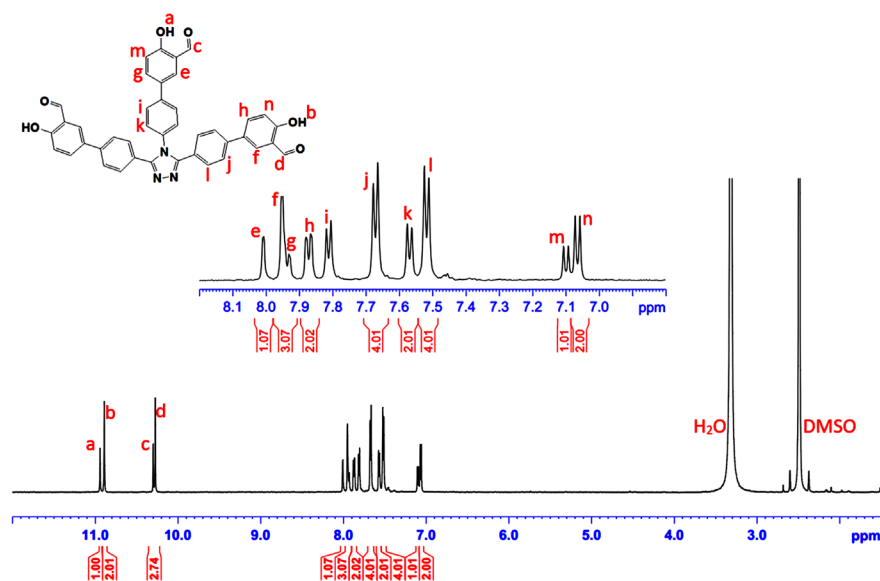


Figure S5. ¹H NMR spectrum of compound 6.

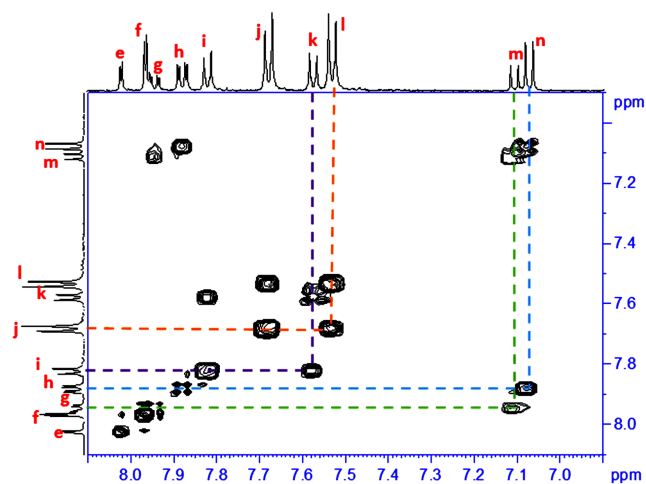


Figure S6. COSY spectrum of compound 6.

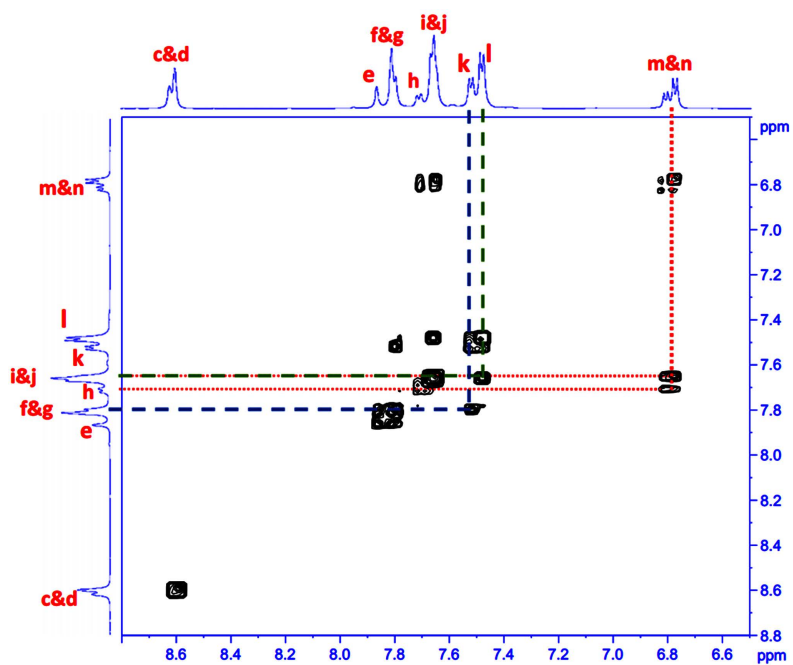


Figure S7. COSY spectrum of TAZS.

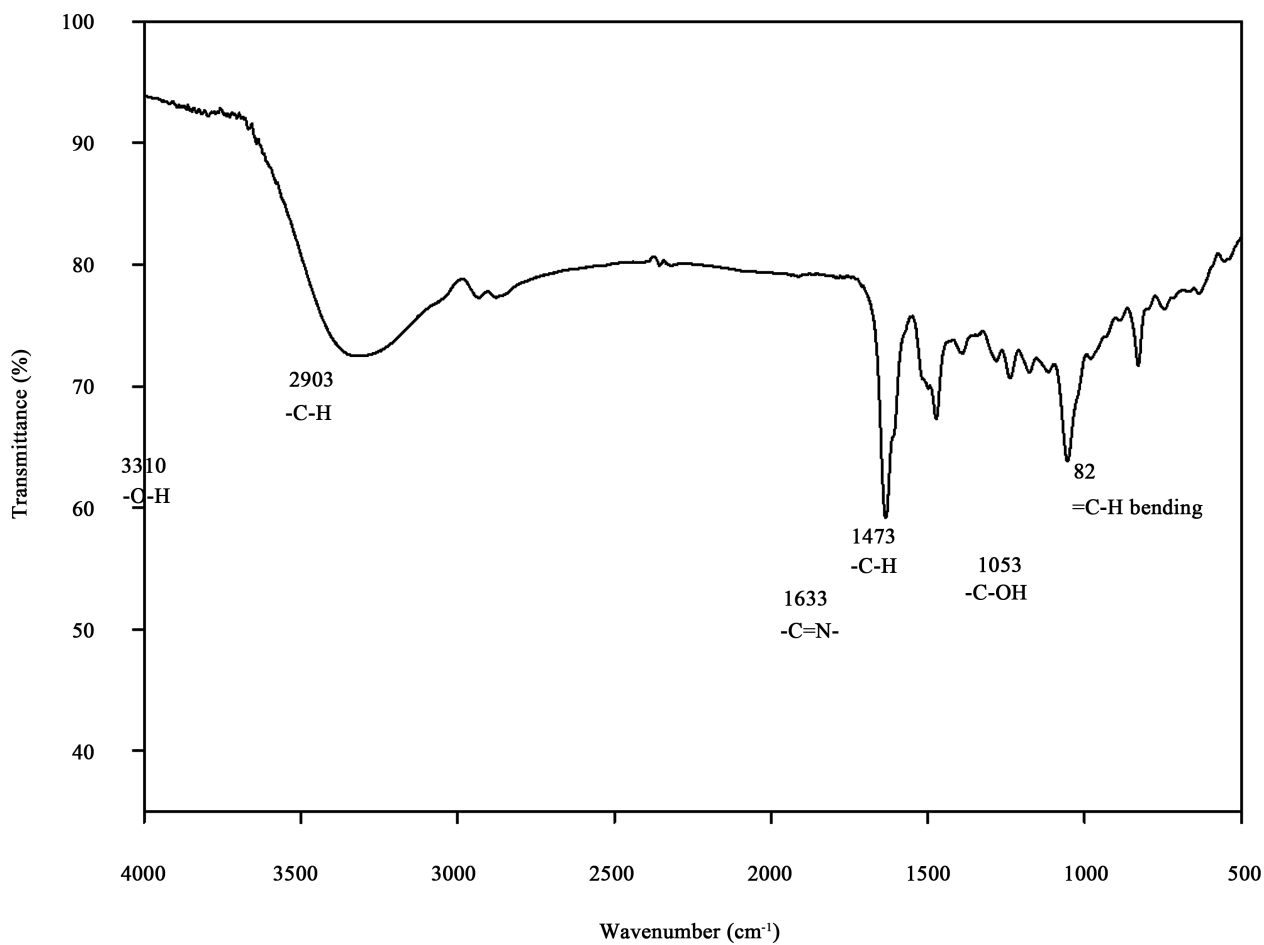


Figure S8. FT-IR spectrum of TAZS.

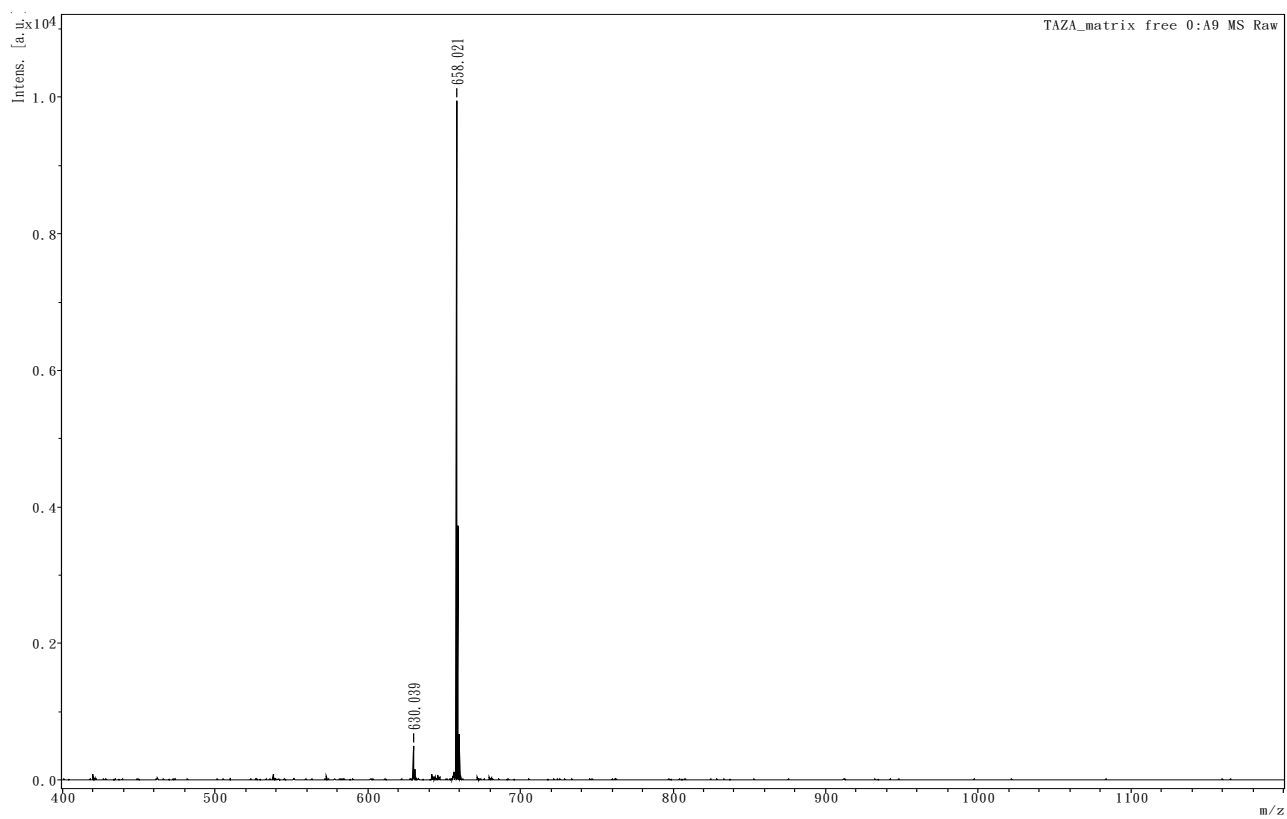


Figure S9. Mass spectrum of compound 6.

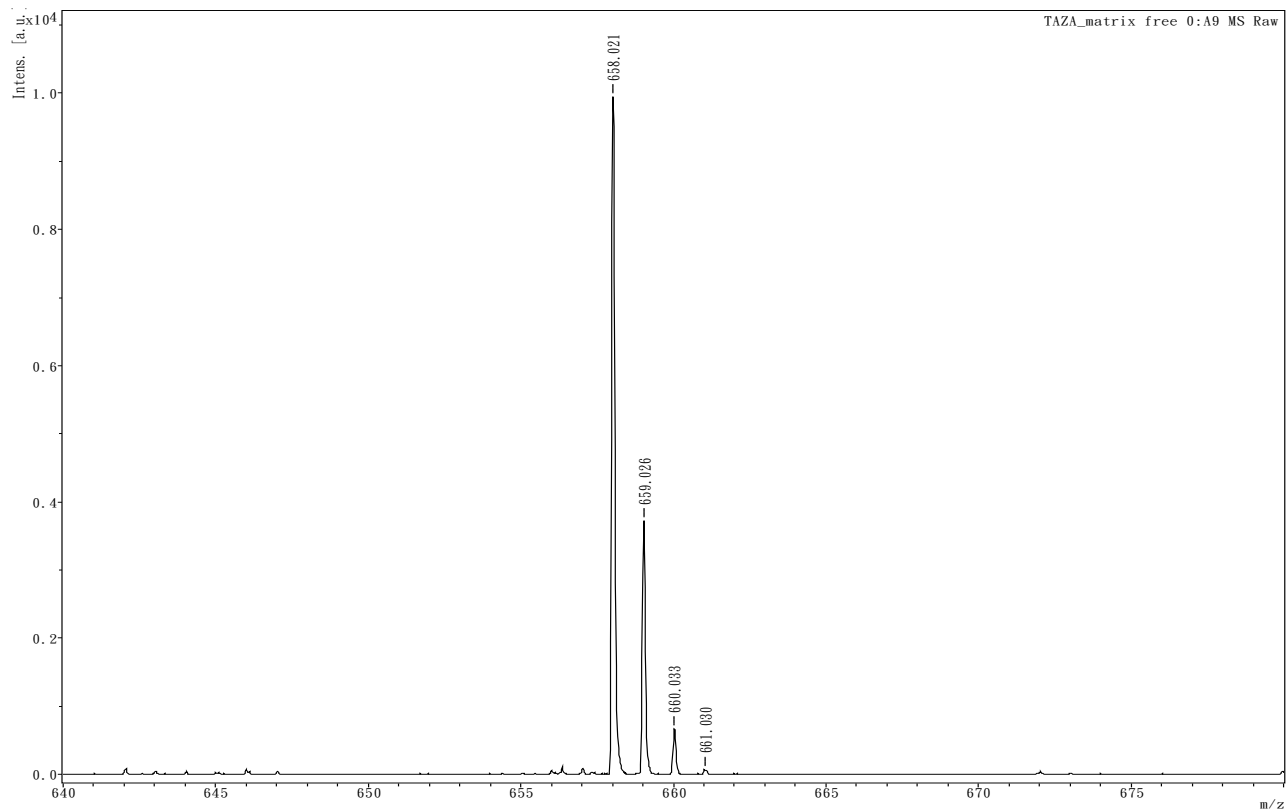


Figure S10. Mass spectrum of compound 6.

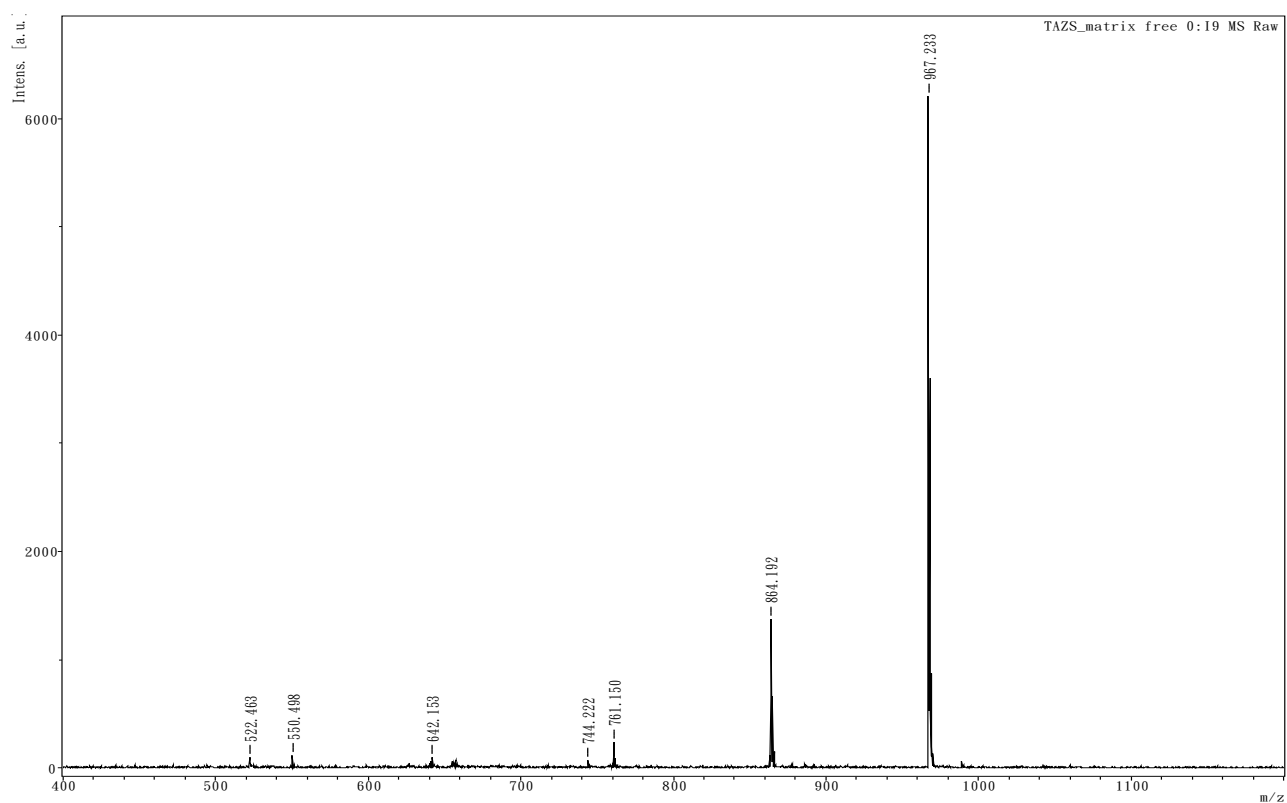


Figure S11. Mass spectrum of TAZS.

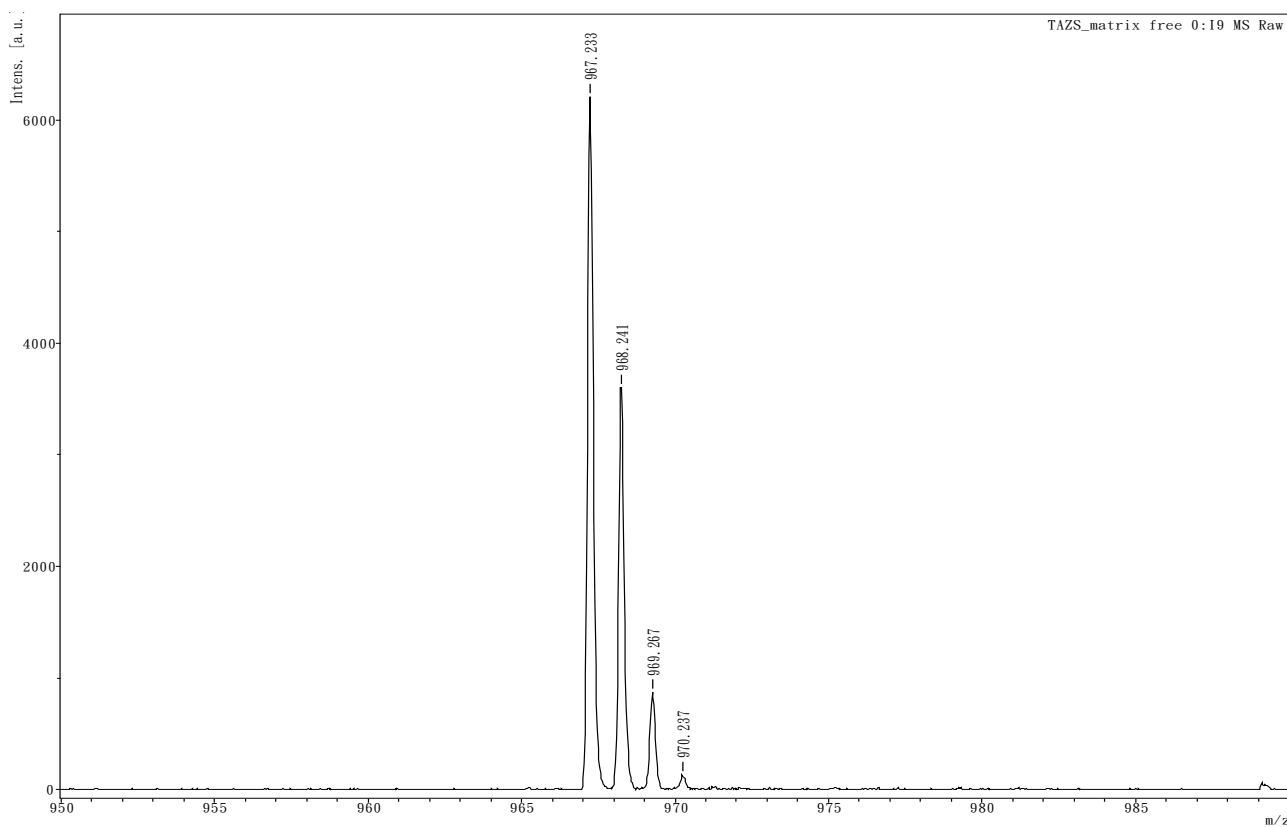


Figure S12. Mass spectrum of TAZS.

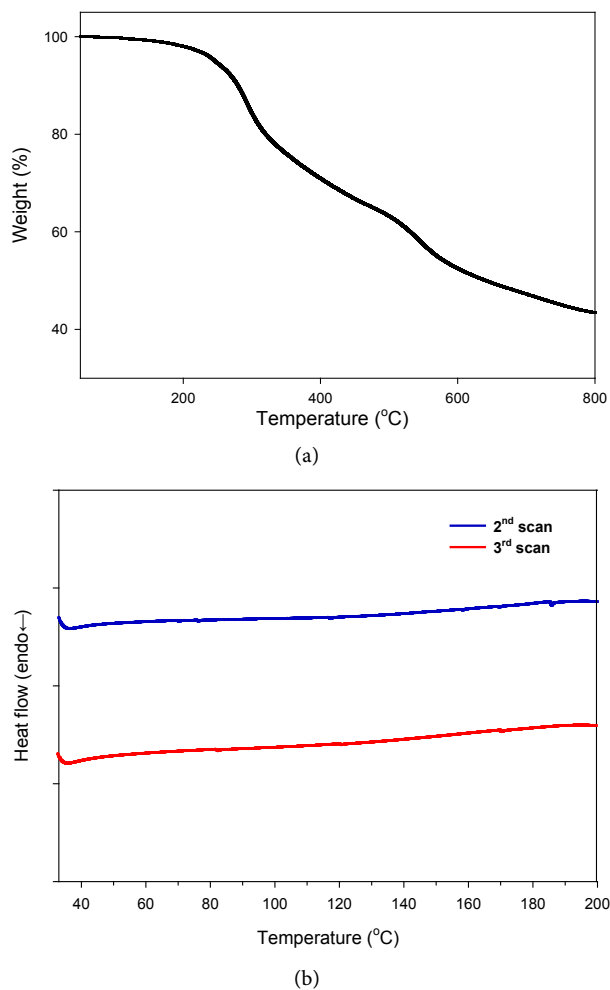


Figure S13. (a) Thermogravimetric curves of TAZS at heating rate of 10 °C/min under nitrogen system. (b) Differential scanning calorimetric curves of TAZS at a heating rate of 10 °C/min.

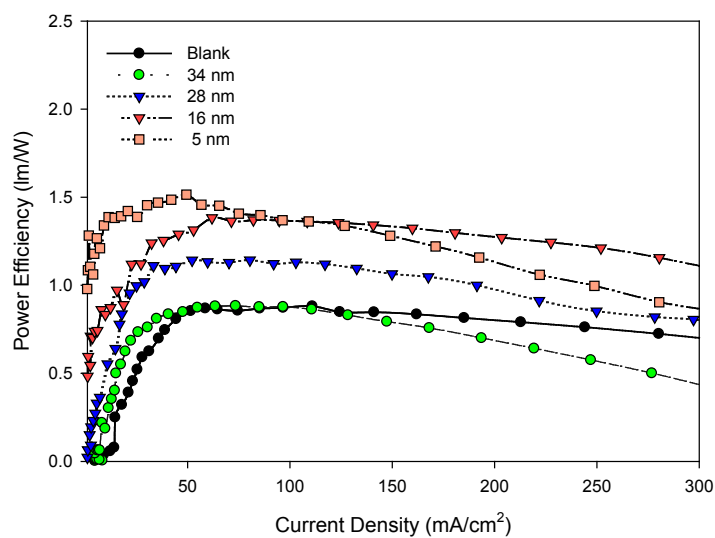


Figure S14. Power efficiency versus current density of PLEDs. Device structure: ITO/PEDOT: PSS (40 nm)/TAZS (x nm)/SY (70 nm)/LiF (1 nm)/Al (90 nm).